International Journal of Material Forming (2021) 14:19–37
https://doi.org/10.1007/s12289-020-01540-5

IJMF 10TH ANNIVERSARY - ADVANCES IN COMPOSITES FORMING AND THEIR INDUCED...

Numerical and experimental investigation of out-of-plane fiber waviness on the mechanical properties of composite materials

M. Thor[1,4] · U. Mandel[2] · M. Nagler[1] · F. Maier[1] · J. Tauchner[3] · M. G. R. Sause[4] · R. M. Hinterhölzl[1]

Received: 8 August 2019 / Accepted: 17 January 2020 / Published online: 25 January 2020

Abstract

The limited capability to predict material failure in composite materials and specifically in wavy composite layers has led to high margins of safety for the design of composite structures. Thus, the full lightweight potential of this class of materials is left unused. To understand the complex failure behavior of composite materials containing out-of-plane fiber waviness under compressive and tensile loading, a non-linear 2D material model was implemented in ABAQUS and validated with extensive experimental test data from compression and tensile tests. Each test was recorded by a stereo camera system for digital image correlation to resolve damage initiation and propagation in detail. This study has shown excellent agreement of numerical simulations with experimental data. In a virtual testing approach various parameters, i.e. amplitude, wavelength and laminate thickness, have been studied. It was found that the failure mode changed from delamination to kink shear band formation with increasing laminate thickness. The wavelength has shown minor influences compared to amplitude and laminate thickness.

Keywords Composite materials · Effects of defects · Fiber waviness · Continuum damage model · Digital image correlation

Introduction

Fiber-reinforced composite materials allow for a significant reduction in weight due to the comparably low density (c.f. 4–5 times less than steel) and, in addition, fibers can be aligned in accordance with to the load paths. This possibility of alignment allows to place the fibers exactly at the position where they are needed to provide the component with its needed stiffness and strength. However, this can lead to a load path-optimized composite structure, not necessarily manufacturable in a robust and defect-free way.

The placement of the fibers or semi-finished textile products is still often carried out by hand, especially in the aviation industry. This allows diverse draping of the unidirectional (UD) layers, woven textiles or non-crimped fabrics (NCF) into the production tool. However, manufacturing effects such as fiber waviness, porosity, delamination and distortion cannot be completely avoided. The increased demand for composite parts for the aviation and automotive industries requires a transition to (partially) automated manufacturing processes. Those systems come with a higher deposition rate and ensure reproducible quality, but also imply production effects, e.g.

✉ M. Thor
michael.thor@fh-wels.at; https://www.fh-ooe.at/en/

U. Mandel
https://www.lcc.mw.tum.de/en/home/

M. Nagler
https://www.fh-ooe.at/en/

F. Maier
https://www.fh-ooe.at/en/

J. Tauchner
https://www.facc.com/en/

M. G. R. Sause
http://www.mrm.uni-augsburg.de/en/

R. M. Hinterhölzl
https://www.fh-ooe.at/en/

[1] Research Group of Lightweight Design and Composite Materials, University of Applied Sciences Upper Austria, Stelzhamerstraße 23, 4600 Wels, Austria

[2] Institute for Carbon Composites, Technical University of Munich, Boltzmannstraße 15, 85748 Garching b, München, Germany

[3] FACC Operations GmbH, Fischerstrasse 9, 4910 Ried im Innkreis, Austria

[4] Institute of Materials Resource Management, University of Augsburg, Universitätsstraße 1 Nord, 86159 Augsburg, Germany

fiber waviness [1, 2]. This necessitates a well-founded understanding of those implicit effects on the mechanical properties of the manufactured structure.

Wave description and influence parameter

Fiber waviness is denoted as a wave-formed ply and/or fiber deviation from a straight alignment in a unidirectional laminate. Wavy plies can appear in arbitrary shapes and locations and can principally be classified into in-plane and out-of-plane waves, whereas Nelson et al. [3] stated, that both show similar strength degradations.

In general, the shape of fiber waviness is described by the ratio of amplitude to wavelength. Davidson and Waas [4] introduced 6 parameters to characterize the wave, indirectly including the laminate thickness. While amplitude A and wavelength L are most commonly used to describe the wave (Fig.1), the maximum deviation θ_{max} is considered to have the greatest impact on the mechanical properties.

Important influencing parameters such as maximum deviation of the fiber orientation from the original orientation, as well as the laminate thickness, have received little attention in previous investigations. The wave pattern is typically represented mathematically as sinusoidal waves [5, 6]. El-Hajjar and Petersen [7] used a Gaussian function to capture the bell curve of wavy plies, which was found to better represent the wave geometry. Further, a more outward lying wavy layer leads to a greater decrease in strength, since the layers on the edge of the laminate are supported only one-sided and therefore fail earlier [8].

As the matrix properties and especially the thereby caused shear nonlinearity of the composite plays a dominant role in the failure behavior of wavy layers in composites, hot-wet conditioning (typically 70 °C and 85% relative humidity in aviation industry) is also considered to substantially influence this behavior.

For a good prediction quality, the geometry of the fiber waviness must be reproduced as exactly as possible or in its stochastic deviation. Creighton et al. [9] and Sutcliffe et al. [10] have captured the fiber orientation and its scattering by means of digital image analysis. Nikishkov et al. [11] investigated automated FE mesh generation based on CT images.

Occurrence and assessment of fiber waviness

The origins of fiber waviness are manifold and a good overview is given in [1, 2]. Some relevant sources are the draping step of the layers whether by hand or automated, compacting the layers in the autoclave or in the RTM tool [12, 13], and gaps, overlaps, bridging and fiber steering in the AFP process [14, 15].

Those effects cannot be completely avoided and therefore have to be tolerated and be considered as an inherent part of the structure. Fiber waviness can be considered as one of the most significant effects occurring in composite materials, due to the severe knockdown effect on the mechanical properties, such as stiffness, strength and fatigue and therefore, dramatically reduces the load carrying capacity of the material. If these unwanted irregularities are categorized as manufacturing features, i.e. effects, or defects, depends on the size, amount, and location of the effects in the component. On one side, the strength and stiffness reserve at the location of the feature and on the other side functional requirements, e.g. water tightness, have to be taken into account. The assessment of manufacturing effects further depends on the industry. In aircraft industry, the allowance limits for defects are very restricted, while in the automotive industry the requirement of short cycle times lead to a trade-off between robust processes and tolerated manufacturing imperfections.

To this point, there is still no generic acceptable approach to quantitatively support accept/reject/repair-decisions and make a consistent assessment of wavy layers in composites. If the feature is decided to be a defect, typically a deviation from design must be requested in aviation industry and an individual decision must be made on “use as is”, repair or rejection. In some cases representative experiments on subcomponent-level are performed on a statistical basis, however, this is both time consuming and cost intensive.

Therefore, it is necessary to strive for a fiber-, and especially a manufacturing-oriented design and construction of composite components. Towards this goal, design and production

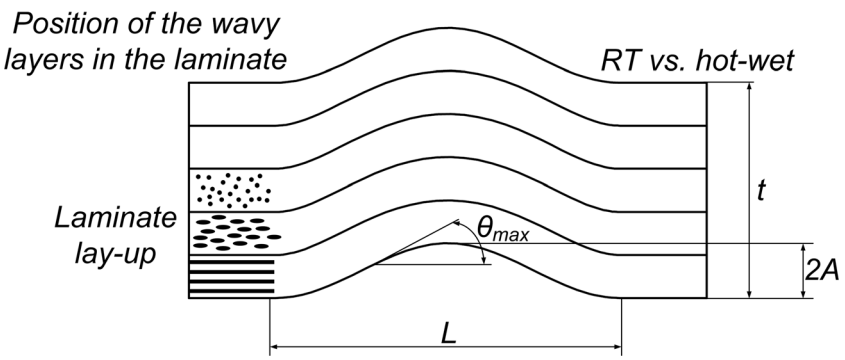

Fig. 1 Parameters influencing the mechanical properties, e.g. amplitude A, wavelength L, laminate thickness t, maximum fiber misalignment angle θ_{max}, environmental conditions (room temperature or hot-wet), layup and the position of wavy layers within the laminate

engineers aim to expand the permissible margin of safety by assessing the effect on stiffness and strength of those production effects, i.e. fiber waviness, porosity, delamination etc.. Additionally, they aim to reduce, or in the best case avoid, them on the process side, increasingly with the help of process simulations such as in [16–18].

Mechanical response of wavy composites

Even simple global loading cases, e.g. uniaxial extension, of wavy layers in a composite material locally induce a complex three-dimensional stress state consisting of a combination of interlaminar normal and shear stresses. Interlaminar tensile stresses normal to the lamina plane are induced as a consequence of transverse strains caused by the wave geometry [19]. Groundbreaking experimental and analytical studies on the influence of fiber waviness on mechanical properties were performed by Hsiao and Daniel [5, 20] and Piggott [21].

It has been shown that compressive strength and stiffness are especially sensitive to the presence of fiber waviness. The initial misalignment can decrease the compressive strength by up to 60% [22].

Experimental studies under compression load for fiber waviness were carried out by [23–26], all reporting a significant reduction on compression properties. Lemanski and Sutcliffe [27] numerically investigated the influence of fiber waviness under compression load. It was shown that the compressive strength falls rapidly with the proportion of laminate width covered by the wavy region. The effect of length and position of the wavy region was found to have a smaller effect on the compressive strength. Zhu et al. [28] developed a three-dimensional analytical method based on the classical lamination theory. Li et al. [29] have dealt with the determination of the reduced stiffness due to fiber waviness by proposing a micro-sphere based homogenization approach.

In a numerical and experimental study conducted by Vogler et al. [30] a strong interaction between compressive and shear stresses on compressive strength could be demonstrated. The general failure behavior of composites under compression and its resulting failure mechanisms, i.e. elastic microbuckling, plastic microbuckling, delaminations, fiber crushing and longitudinal cracking, have been studied in [4, 30–38], and similar mechanisms can be observed in composites containing fiber waviness. It has been shown that the nonlinear matrix properties dominate the damage initiation and the stiffness and strength decrease [22, 39].

The formation of a shear kink-band is induced by local fiber buckling or matrix flow induced by initial or as-delivered fiber misalignments in the UD material, which continue to rotate under load. In the case of fiber waviness, this effect is further intensified due to the characteristics of the waviness. A very detailed study on experimental, analytical and numerical aspects on the formation of kink-bands can be found in [40, 41]. Davidson and Waas [4] have shown that under compression load this is the critical failure mode also for laminates containing fiber waviness. They used a local-global approach, where the local FE-based micromechanical analyses for fiber kinking are integrated into the global macroscopic FE model of fiber waviness, which exactly maps the geometry of the fiber waviness. The World-Wide Failure Exercise of Hinton et al. [42] have shown that the failure criteria show significant weaknesses, partly due to not considering fiber kinking under combined compression and shear stresses.

Under tensile loading, the fibers are pulled “straight”, resulting in a stiffening effect and a failure of the interface between fiber and matrix due to local interlaminar normal and shear stresses and finally to delamination [43, 44].

For shear loading in the laminate plane of a laminate with fiber waviness, few experimental and simulative investigations are known. In the few available literature references [15, 45] an influence of up to 12% on the reduction of the shear strength is determined. Similar to shear stresses in laminates without fiber waviness [46], a strong influence of the nonlinear shear behavior on the failure process is assumed for laminates containing fiber waviness.

In recent publications the simulations are validated on strain field measurement to record damage initiation and progression [4, 47]. Previous studies have mainly focused on UD laminates, all oriented in the same direction, and have concentrated on the effect of fiber waviness on the stiffness. Quasi-isotropic (QI) laminates containing wavy layers have been rarely investigated so far. Mukhopadhyay et al. published work on compressive [48], tensile [49] and fatigue behavior [50] of QI laminates containing embedded wrinkles using 3D finite element modelling approaches reporting a more complex failure behavior due to multiple active damage mechanisms and their interaction.

The study of Wilhelmsson et al. [51] has shown a considerable influence of embedded out-of-plane waviness on the bending during compression testing.

This study aims to investigate the mechanical behavior of out-of-plane fiber waviness of both unidirectional and quasi-isotropic laminates by numerically simulating damage initiation and propagation, using a custom material model, implemented in ABAQUS/Explicit [52]. To determine material parameter and validate our simulations we conducted uniaxial compression and tensile tests supported by optical strain field measurements.

Constitutive material behavior

The constitutive material behavior of a single UD ply can be modelled by an undamaged non-linear elasto-plastic hardening regime and an elasto-damage softening regime shown in

Fig. 2. In the hardening regime the stress increases with ascending strain. The degree of non-linearity depends on the angle between loading direction and orientation of the layer. The failure criterion according to Puck [53] is used to determine the damage initiation. The degradation of the continuum is described in the softening regime and controlled by energy-based linear stiffness degradation. Modelling of interface delamination, e.g. cohesive zone modelling (CZM) or virtual crack closure technique (VCCT), is not part of the model. For laminates with all plies in 0°-direction the use of a 2D model in combination with a plain strain assumption has been validated in [22]. Testing the applicability of this approach for QI laminates is still an open task and part of this current study.

Non-linearity in the elasto-plastic hardening regime

A plasticity model developed by Sun and Chen [54] is implemented to describe the non-linear constitutive behavior of a IM7 unidirectional carbon fiber reinforcement embedded in a 8552 thermosetting epoxy matrix. The plasticity model (plastic potential) is based on a quadratic yield function $f(\sigma_{ij})$, defined in terms of the stress components σ_{ij} in the principal material directions.

The plastic potential is expressed by the general yield function

$$2f = \sigma_{33}^2 + 2a_{66}\sigma_{13}^2 \tag{1}$$

where the material constant a_{66} describes the anisotropy in the plasticity.

The incremental strain $d\varepsilon_{ij}$ can be decomposed into an elastic strain component $d\varepsilon_{ij}^e$ and a plastic strain component $d\varepsilon_{ij}^p$

$$d\varepsilon_{ij} = d\varepsilon_{ij}^e + d\varepsilon_{ij}^p. \tag{2}$$

The in-plane incremental plastic strain components $d\varepsilon_{ij}^p$ are defined in terms of the in-plane yield function f and the plastic multiplier $d\lambda$ via the associated flow rule. Assuming that the longitudinal plastic strain increment $d\varepsilon_{11}^p$ can be neglected since most unidirectional composite materials behave almost linear elastic in longitudinal tension and compression loading [54] the plastic strain component can be described as

$$d\varepsilon_{ij}^p = \begin{Bmatrix} d\varepsilon_{11}^p \\ d\varepsilon_{33}^p \\ d\gamma_{13}^p \end{Bmatrix} = \frac{\partial f}{\partial \sigma_{ij}} d\lambda = \begin{Bmatrix} 0 \\ \sigma_{33} \\ 2\, a_{66}\, \sigma_{13} \end{Bmatrix} d\lambda, \tag{3}$$

where γ_{13} denotes the engineering shear strain.

Similarly, the work per unit volume dW performed during elongation $d\varepsilon_{ij}$ can be also decomposed into a reversible elastic work dW^e and an irreversible plastic work dW^p. The incremental plastic work dW^p is defined as

$$dW^p = \sigma_{ij} d\varepsilon_{ij}^p = 2f d\lambda. \tag{4}$$

By introducing the effective stress $\overline{\sigma} = \sqrt{3f}$ for the case of a plane stress state, the plastic work increment dW^p can be written as

$$dW^p = \overline{\sigma}\, d\overline{\varepsilon}^p. \tag{5}$$

Rewriting in terms of the effective plastic strain increment $d\overline{\varepsilon}^p$ leads to

$$d\overline{\varepsilon}^p = \frac{2}{3}\overline{\sigma}\, d\lambda = \sqrt{\frac{2}{3}\left(\sigma_{33}^2 + 2a_{66}\sigma_{13}^2\right)} d\lambda. \tag{6}$$

The incremental plastic stress-strain relation only depends on the values of the plasticity coefficient a_{66} and the plastic multiplier $d\lambda$ which is calculated as

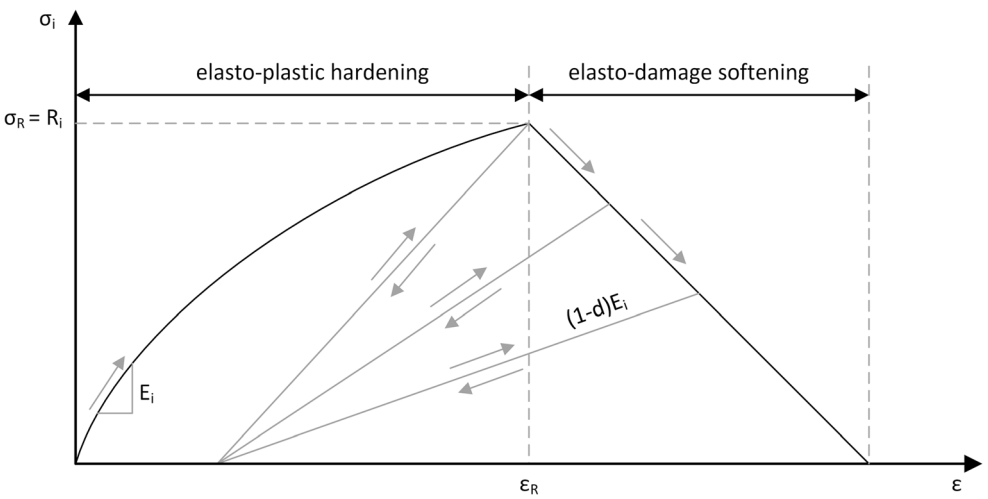

Fig. 2 Nonlinear elasto-plastic hardening and elasto-damage softening

$$d\lambda = \frac{\left(\frac{\partial f}{\partial \boldsymbol{\sigma}}\right)^T \boldsymbol{C^0} d\boldsymbol{\varepsilon}}{\frac{4}{9}\overline{\boldsymbol{\sigma}}^2 H_p + \left(\frac{\partial f}{\partial \boldsymbol{\sigma}}\right)^T \boldsymbol{C^0} \frac{\partial f}{\partial \boldsymbol{\sigma}}} \tag{7}$$

with the plastic modulus H_p

$$H_p = \frac{d\overline{\boldsymbol{\sigma}}}{d\overline{\boldsymbol{\varepsilon}}^p} = \frac{1}{n_{nl} A_{nl}} \left(\frac{\overline{\boldsymbol{\varepsilon}}^p}{A_{nl}}\right)^{\frac{1-n_{nl}}{n_{nl}}}. \tag{8}$$

H_p is a derivative of the effective stress with respect to the effective plastic strain and using the current effective plastic strain.

Fiber composites are assumed to have no clear yield locus. For this reason, a power law approach can be used to describe the non-linear constitutive behavior in order to fit a master curve of equivalent stress over equivalent strain. The compression and tension regimes must be considered independently of each other.

$$\overline{\boldsymbol{\varepsilon}}^p = A_{nl}\, \overline{\boldsymbol{\sigma}}^{n_{nl}} \tag{9}$$

For a complete description of the non-linear material behavior, the parameter a_{66} must be obtained from off-axis tests (OAT).

In the plane stress state, the prevailing stresses can be indicated as follows

$$\boldsymbol{\sigma} = [\sigma_{11}, \sigma_{33}, \sigma_{13}]^T, \tag{10}$$

with the associated strains

$$\boldsymbol{\varepsilon} = [\varepsilon_{11}, \varepsilon_{33}, \varepsilon_{13}]^T. \tag{11}$$

Assuming a purely elastic material behavior, stress and strain can be related by means of Hook's law (linear elastic material law) by introducing the material stiffness matrix, respectively compliance matrix. In Voigt notation in combination with Einstein's summation convention follows.

$$\begin{aligned} \sigma = C^0 \varepsilon &\rightarrow \sigma_i = C^0_{ij} \varepsilon_j \\ \varepsilon = S^0 \sigma &\rightarrow \varepsilon_i = S^0_{ij} \varepsilon_j \end{aligned} \tag{12}$$

For the plane stress state, the stiffness matrix C^0_{ij} can be defined as

$$C^0_{ij} = \frac{1}{1-\nu_{13}\nu_{31}} \begin{bmatrix} E_1 & \nu_{31}E_1 & 0 \\ \nu_{13}E_3 & E_3 & 0 \\ 0 & 0 & (1-\nu_{13}\nu_{31})G_{13} \end{bmatrix}. \tag{13}$$

The corresponding compliance matrix S^0_{ij} is written as

$$S^0_{ij} = \begin{bmatrix} \frac{1}{E_1} & -\frac{\nu_{13}}{E_1} & 0 \\ -\frac{\nu_{31}}{E_3} & \frac{1}{E_3} & 0 \\ 0 & 0 & \frac{1}{G_{13}} \end{bmatrix}. \tag{14}$$

Continuum damage model

Damage variables

In the case of damage progression in the lamina, the constitutive relationship resulting from the progressive damage is considered in the form of a reduction of the stiffness matrix. In this case, a pure elasto-damage is assumed. A damage variable d was introduced in the form of a thermodynamic state variable to determine the damage progression. In the general anisotropic case, the damage of fiber composites is described in the form of a 4th order damage tensor $\boldsymbol{D}$. In addition, a 4th order damage influence tensor $\boldsymbol{M}(\boldsymbol{D})$ is introduced to characterize the damage condition. Applied to the concept of the equivalence of stresses, the effective stresses in the damaged continuum can thus be written as

$$\widetilde{\boldsymbol{\sigma}} = \boldsymbol{M}(\boldsymbol{D})\boldsymbol{\sigma} \tag{15}$$

with

$$\boldsymbol{M}(\boldsymbol{D}) = (\boldsymbol{I} - \boldsymbol{D})^{-1} \tag{16}$$

wherein $\boldsymbol{I}$ represents the 4th order unit tensor. In the case of an uncoupled damage and a unilateral damage propagation in the direction that tears equivalent to the fiber or matrix direction, the damage tensor $\boldsymbol{D}$ can be written for the pane stress state

$$\boldsymbol{D} = \begin{bmatrix} d_{11} & 0 & 0 \\ 0 & d_{33} & 0 \\ 0 & 0 & d_{13} \end{bmatrix} = \begin{bmatrix} d_f & 0 & 0 \\ 0 & d_m & 0 \\ 0 & 0 & d_s \end{bmatrix} \tag{17}$$

wherein 1 and 3 denote the fiber and matrix direction, respectively. This allows the damage influence tensor $\boldsymbol{M}(\boldsymbol{D})$ to be specified.

$$\boldsymbol{M}(\boldsymbol{D}) = \begin{bmatrix} \frac{1}{1-d_{11}} & 0 & 0 \\ 0 & \frac{1}{1-d_{33}} & 0 \\ 0 & 0 & \frac{1}{1-d_{13}} \end{bmatrix} \tag{18}$$

In the case of material damage in the continuum mechanics, the damage variable d is introduced as a thermodynamic

state variable. The evolution of the damaged stiffness matrix by internal state variables d are schematically shown in Fig. 3 for transverse direction. The free energy potential f^d can be defined as a function of d. For the damage process free of thermal influence, the following should therefore apply

$$f^d = f^d\left(\varepsilon_{ij}, d\right) \tag{19}$$

$$\dot{f^d} = \frac{\partial f^d}{\partial \varepsilon_{ij}}\dot{\varepsilon_{ij}} + \frac{\partial f^d}{\partial d}\dot{d} \tag{20}$$

$$\Delta = \left(\sigma_{ij} - \frac{\partial f^d}{\partial \varepsilon_{ij}}\right)\dot{\varepsilon_{ij}} - \frac{\partial f^d}{\partial d}\dot{d} \geq 0. \tag{21}$$

The strain equivalence approach can be used to define

$$\varepsilon = \frac{\widetilde{\sigma}}{\boldsymbol{C^0}} = \frac{\boldsymbol{M(D)\sigma}}{\boldsymbol{C^0}} \tag{22}$$

It finally follows for the damaged stiffness matrix $\boldsymbol{C^d(D)}$

$$\boldsymbol{C^d(D) = M^{-1}(D)C^0}$$

$$= \begin{bmatrix} \frac{(1-d_{11})E_1}{1-(1-d_{11})(1-d_{33})\nu_{13}\nu_{31}} & \frac{(1-d_{11})(1-d_{33})\nu_{31}E_1}{1-(1-d_{11})(1-d_{33})\nu_{13}\nu_{31}} & 0 \\ \frac{(1-d_{11})(1-d_{33})\nu_{13}E_3}{1-(1-d_{11})(1-d_{33})\nu_{13}\nu_{31}} & \frac{(1-d_{33})E_3}{1-(1-d_{11})(1-d_{33})\nu_{13}\nu_{31}} & 0 \\ 0 & 0 & (1-d_{13})G_{13} \end{bmatrix} \tag{23}$$

and the elasto-damaged material law

$$\boldsymbol{\sigma(D)} = \boldsymbol{C^d(D)}\varepsilon. \tag{24}$$

The damaged compliance matrix $\boldsymbol{S^d(D)}$ results equivalent to

$$\boldsymbol{S^d(D) = M(D)S^0} = \begin{bmatrix} \frac{1}{(1-d_{11})E_1} & -\frac{\nu_{13}}{E_1} & 0 \\ -\frac{\nu_{31}}{E_3} & \frac{1}{(1-d_{33})E_3} & 0 \\ 0 & 0 & \frac{1}{(1-d_{13})G_{13}} \end{bmatrix}. \tag{25}$$

The dissipation inequality for the damaged material behavior results in two conditions. According to Coleman and Gurtin [55], it applies as for the undamaged material

$$\sigma_{ij}\left(d_{ij}\right) = \frac{\partial f^d}{\partial \varepsilon_{ij}}. \tag{26}$$

Thus, the following condition can be derived from the dissipation inequality, which must be fulfilled for the inequality to apply

$$-\frac{\partial f^d}{\partial D}\dot{D} \geq 0. \tag{27}$$

The term $\frac{\partial f^d}{\partial D}$ corresponds to the energy release as a result of progressive damage to the material. This term is called energy release rate Y and an energetically conjugated quantity of the damage variable.

$$Y(\varepsilon, \boldsymbol{D}) = \frac{\partial f^d}{\partial D} \tag{28}$$

$Y\dot{D}$ describes the energy dissipation rate in the material, where Y is the thermodynamic force and $\dot{D}$ is the thermodynamic flow.

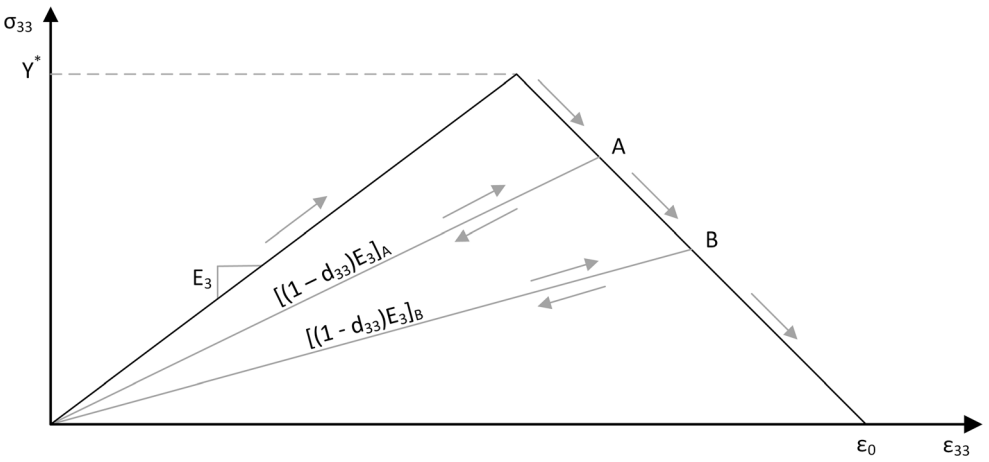

Fig. 3 Damaged stiffness matrix by internal state variables d in transverse direction

Damage initiation

For the damage initiation the well-established Puck criterion [53] is used. The individual failure modes defined by Puck determine the progress of the damage.

Fiber failure under tension $\overline{\sigma_1} \geq 0$

$$f_{EFF}^{t}\left(\overline{\sigma_1}\right) = \frac{\overline{\sigma_1}}{R_{\parallel}^{t}} \leq 0 \tag{29}$$

Fiber failure under compression $\overline{\sigma_1} < 0$

$$f_{EFF}^{c}\left(\overline{\sigma_1}\right) = \frac{\overline{\sigma_1}}{\left(-R_{\parallel}^{c}\right)} \leq 0 \tag{30}$$

Inter-fiber failure under tension $\overline{\sigma_3} \geq 0$ (Mode A)

$$f_{EIFF}^{t}\left(\overline{\sigma_3^t}, \overline{\tau_{31}}\right) = \sqrt{\left[\left(\frac{1}{R_{\perp}^{t}} - \frac{p_{\perp\parallel}^{t}}{R_{\perp\parallel}}\right)\overline{\sigma_3^t}\right]^2 + \left(\frac{\overline{\tau_{31}}}{R_{\perp\parallel}}\right)^2} + \frac{p_{\perp\parallel}^{t}}{R_{\perp\parallel}}\overline{\sigma_3^t} \leq 0 \tag{31}$$

Inter-fiber failure under compression $\overline{\sigma_3} < 0$ (Mode B)

$$f_{EIFF}^{c}\left(\overline{\sigma_3^c}, \overline{\tau_{31}}\right) = \sqrt{\left(\frac{p_{\perp\parallel}^{c}}{R_{\perp\parallel}}\overline{\sigma_3^c}\right)^2 + \left(\frac{\overline{\tau_{31}}}{R_{\perp\parallel}}\right)^2} + \frac{p_{\perp\parallel}^{c}}{R_{\perp\parallel}}\overline{\sigma_3^c} \leq 0 \tag{32}$$

Inter-fiber failure under compression $\overline{\sigma_3} < 0$ (Mode C)

$$f_{EIFF}^{c}\left(\overline{\sigma_3^c}, \overline{\tau_{31}}\right) = \left[\left(\frac{\overline{\tau_{31}}}{2\left(1 + p_{\perp\perp}^{c}\right)R_{\perp\parallel}}\right)^2 + \left(\frac{\overline{\sigma_3^c}}{R_{\perp}^{c}}\right)^2\right]\frac{R_{\perp}^{c}}{-\sigma_3^c} \leq 0 \tag{33}$$

Damage evolution law

The components of the damage tensor $\boldsymbol{D}$, i.e. d_{11}, d_{33}, d_{13}, individually degrade the longitudinal, transverse and shear stiffness, respectively. Since the effects of the damage behave differently under compressive or tensile loading, a total of 5 different damage variables must be determined $\left(d_{11}^{t}, d_{11}^{c}, d_{33}^{t}, d_{33}^{c}, d_{13}\right)$. For simplification, linear approaches for the damage evolution are applied.

The linear approach for the constitutive relationship of the material in the softening regime results in

$$\sigma(\varepsilon) = \sigma_R - K(\varepsilon - \varepsilon_0) \tag{34}$$

where K characterizes the descent in the softening regime.

The damage evolution law is based on the concept of effective stresses in the context of strain equivalence as shown in Fig. 4. The approach applies to uniaxial stress, where f_{Ei} is the stress exposure related to a stress state in the undamaged continua.

$$d_i = 1 + \frac{K_i}{E_i} - \frac{1}{\left(f_E(\tilde{\sigma})\right)_i}\left(1 + \frac{K_i}{E_i}\right) \quad i = [11^t,\ 11^c,\ 33^t,\ 33^c,\ 13] \tag{35}$$

This definition is used to determine the damage progression as a function of the effective stresses.

Energy consideration and element size regularization

In continuum damage approaches the damage is represented non-locally, i.e. related to a unit volume (continuum) homogenized in the constitutive relationship. Due to the brittle fracture behavior of fiber composites, the formation of macro-cracks due to diffuse micro-damages takes place in a relatively narrow specific area known as the crack process zone (CPZ). In order to enable a relationship between the non-local definition of the continuum damage approach and the local definition of crack formation, the following relationship can be established. The product of the energy density per unit volume with the specific width of the crack process zone corresponds to the fracture energy resulting from the formation of the stress-free crack. In other words, the dissipated energy for the complete deterioration of the material in terms of a unit volume is equal to the dissipated energy for crack development in terms of a unit area.

$$G_f = g_f L_{CPZ} \tag{36}$$

Since the quantities in this equation represent all intrinsic material parameters, the numerical FE consideration would have to be discretized in such a way that the element size corresponds to the intrinsic width of the crack process zone. In the consideration of damage processes of fiber composite materials this procedure is not useful. Therefore, a new mesh-related width parameter l^* is introduced, which is no longer bound to the physical width of the crack process zone, but represents a regularized numerically defined quantity. By adjusting the area under the stress-strain curve, a dissipated energy in the failed element is obtained as a function of the ratio of physical crack zone width and numerical characteristic element length.

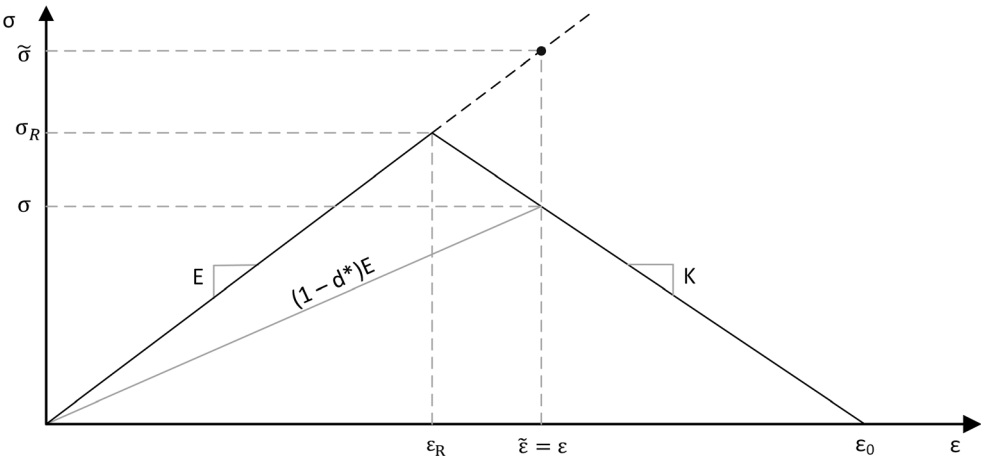

Fig. 4 Damage evolution law based on effective stresses and equivalence of strains

$$W = \frac{G_f}{l^*} \tag{37}$$

$$G_f = \frac{1}{2}\left(\frac{1}{E_i} - \frac{1}{K_i}\right)(R_i)^2 l^* \tag{38}$$

An element size regularization is thus carried out by adjusting the descent in the softening area.

$$K_i = \frac{E_i (R_i)^2 l^*}{2G_i E_i - (R_i)^2 l^*} \tag{39}$$

Both the strength and stiffness are independent material parameters. The fracture energy serves as an intrinsic input parameter. Mode I and II fracture toughness can be empirically determined by material tests using a DCB and ENF test, respectively [56].

Materials and methods

Specimen preparation

The pre-impregnated polymer composite IM7–8552 (Hexcel Corporation, Stamford, USA) is used. The nominal cured ply thickness of the unidirectional (UD) prepreg layer is 0.131 mm, according to the material data sheet. Laminates are fabricated in an autoclave following the recommended curing cycle for monolithic components. Reference specimen (no waviness) thickness is, consistent with test standards, kept at 2.1 mm, i.e. 16 layers of 0° (UD) or with a stacking sequence of $(0/45/-45/90)_{2s}$ for a quasi-isotropic laminate (QI). Specimen containing fiber waves were 5.1 mm, i.e. 40 plies at 0° (UD) or with a stacking sequence of $(0/45/-45/90)_{5s}$ (QI).

Two configurations of sinusoidal waves were realized using a one-side female metal plate tooling in which the defined sinusoidal wave configurations where milled in with a wavelength $L_1 = 27.9$ mm and amplitude $A_1 = 1.19$ mm (wave 1) and $L_2 = 14.5$ mm and $A_2 = 0.58$ mm (wave 2). Laminate quality was verified by measuring the fiber volume fraction (61.3%, 0.95% STD) using wet chemical fiber extraction according to EN 2564 for 12 specimens.

Experimental methods and test set-ups

Tensile and compression testing

Tensile and compression tests are carried out in the spirit of ASTM D3039 and ASTM D6641. Material testing was conducted on universal test machines (Zwick, Ulm, Germany) with a maximum load of 150 kN. The tests were displacement controlled with a rate of 2 mm/min and continued until failure occurred. An overview of the conducted tests is given in Table 1.

Digital image correlation

Digital image correlation (DIC) is a powerful tool to measure the full field strain distributions during mechanical testing of materials. DIC provided information on mechanisms and a full 2D strain field prior to failure, i.e. the location of strain concentrations. However, capturing damage initiation is limited by the (typically lower) frame-rate as well as the detectable size of an event. We used a stereo camera system with two 12 Megapixel cameras (GOM Aramis™ 3D 12 M) equipped with 100 mm lenses. The DIC measurement system was triggered by the test software via analog inputs, ensuring synchronized recording of images with the force and displacement signal. Images

Table 1 Test plan showing configurations and number of specimens

	Loading	No. of specimen	Layup	Dimension (mm)
Wave 1	Compression	5	0°	130 × 10
Wave 2	Compression	5	0°	115 × 10
Wave 1	Compression	5	QI	130 × 25
Wave 2	Compression	5	QI	115 × 25
Wave 1	Tension	5	0°	250 × 10
Planar reference	Compression	5	0°	110 × 10
Planar reference	Compression	5	90°	110 × 10
Planar reference	Tension	5	0°	250 × 10
Planar reference	Tension	5	90	250 × 25
Planar reference	Compression	3	QI	110 × 10
15° Off-axis	Tension	5	15°	250 × 25

were obtained at 10 Hz. A homogeneously distributed speckle pattern was applied on a matt white grounding using the airbrush system Minijet 4400 B RP (SATA, Kornwestheim, Germany). The test-set up is shown in Fig. 5. To analyze the images we used GOM Correlate Professional (2016). The facet size was set to (14 × 14) pixels with an overlap to get a point distance of 10 pixels.

FE model

The finite element model of both the 15° off-axis tests and wavy geometries are modeled with reduced integration plain strain elements (CPE4R) including hourglass control to avoid zero energy modes. For parameter studies a python script was written to automatically build up FE models with varying parameters, e.g. amplitude, wavelength and laminate thickness. The material model described in Section 2 was implemented as a material user-subroutine VUMAT in ABAQUS/Explicit [52]. A representative FE model of a wavy specimen including boundary conditions and loading is shown in Fig. 6. For better visualization, a coarse mesh is shown. Prior to the numerical simulations, a mesh size study was carried out and 35–40 elements in thickness direction were found to be sufficient. Simulation results of the two wave configurations (wave 1 and 2) were compared with experimental test data. A parameter study was carried out for varying amplitudes (0.1A-2A), laminate thicknesses (0.5A-6A), where A denotes the baseline amplitude of 1.19 mm, and wavelengths (13.45–41.35 mm). For modelling quasi-isotropic layups with the 2D approach the material properties were transformed for each orientation according to classical laminate theory and applied to the corresponding layers.

The material properties of IM-7-8552 carbon fiber reinforced epoxy matrix prepreg used for the simulations are given in Table 2. Most simulations were carried out before experimental tests, therefore material parameter from literature were used. These values are consistent with our tested values (c.f. Table 2 and Table 3).

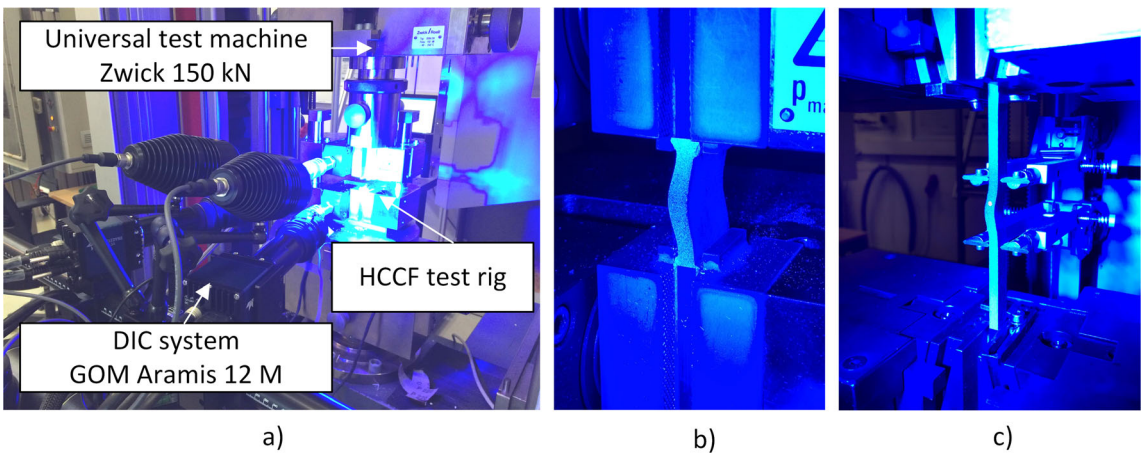

Fig. 5 **a** Mechanical test set-up using DIC and hydraulic composite compression fixture (HCCF); **b** compression specimen; **c** tensile specimen

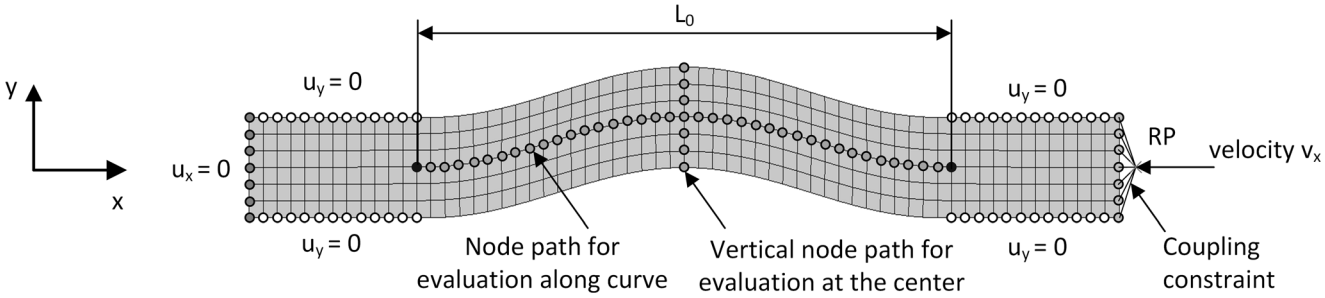

Fig. 6 Representative FE model of wavy compression specimen showing node sets for boundary conditions, loading and evaluation

Results and discussion

Mechanical behavior of planar reference and wavy specimen

The experimental data for planar reference and wavy specimen under compression (Figs. 7 and 8) and tensile loading (Fig. 9) show a non-linear stress strain response for wavy specimen and a considerable knockdown. Young's modulus in fiber direction and the peak-stress before failure for all tests are shown in Table 3. The compressive strength is reduced by approximately 75% for the more pronounced wave configuration (wave 1) and 50% for the less pronounced wave (wave 2). The latter also shows a substantial reduction of the strain-to-failure by approximately 45%. Those results are in good accordance with previously reported findings [22]. Although the compression properties were assumed to be more affected by fiber waviness compared to tensile loading [43, 44], results from mechanical tests on wave 1 show a drop of 70% in tensile strength for first ply failure, where mode I delamination occur due to positive stresses in thickness direction σ_z (Fig. 13c). We found a dramatic drop in compressive strength for both wave configurations with quasi-isotropic laminate compared to the reference specimen. The compressive strength dropped by approximately 65% (wave 1) and 32% (wave 2). Interestingly, we could only observe a reduction in stiffness for the more pronounced wave (wave 1) but not the other one (wave 2). In compression loaded laminates, containing fiber waviness, the mechanical properties of the 90°-layers are not reduced by the wave. The highly affected 0°-layers

Table 2 Material properties for IM7–8552 used for the simulations

Longitudinal stiffness	E_1	171.42	[GPa]	[61]
Transverse stiffness	$E_2 = E_3$	9.08	[GPa]	[61]
Poisson's ratio	$\nu_{12} = \nu_{13}$	0.32	[−]	[61]
	ν_{23}	0.43	[−]	[61]
Shear stiffness	$G_{12} = G_{13}$	5.29	[GPa]	[61]
	G_{23}	3.98	[GPa]	[61]
Longitudinal tension strength	$R_{\parallel}^{t}$	2326.2	[MPa]	[61]
Longitudinal compression strength	$R_{\parallel}^{c}$	1200.1	[MPa]	[61]
Transverse tension strength	$R_{\perp}^{t}$	62.3	[MPa]	[61]
Transverse compression strength	$R_{\perp}^{c}$	255	[MPa]	[58]
Shear strength	$R_{\perp\parallel}$	86	[MPa]	[62]
Inclination parameter	$p_{\perp\parallel}^{t}$	0.35	[−]	[63]
Inclination parameter	$p_{\perp\parallel}^{c}$	0.35	[−]	[63]
Fracture energy in longitudinal tension	$G_{\parallel}^{t}$	133	[kJ/m^2]	*
Fracture energy in longitudinal compression	$G_{\parallel}^{c}$	150	[kJ/m^2]	*
Fracture energy in transversal tension	$G_{\perp}^{t}$	0.277	[kJ/m^2]	[61]
Fracture energy in transversal compression	$G_{\perp}^{c}$	1.31	[kJ/m^2]	[64]
Fracture energy in in-plane shear	$G_{\perp\parallel}$	0.79	[kJ/m^2]	*
Parameter for non-linearity model	a_{66}	2.2		**
Parameter for non-linearity model	A_{nl}	1.2E-14		**
Parameter for non-linearity model	n_{nl}	4.8		**

*Assumed values

**Obtained from experimental data in accordance with [58, 65]

Table 3 Test data of stiffness and strength properties for IM7–8552 planar reference and wavy specimen

	Compression		Tension	
	E_{1c} [GPa]	σ_{cm} [MPa]	E_{1t} [GPa]	σ_{tm} [MPa]
Reference UD	160.6	1322.3	172.9	2094.3
Wave 1 UD	78.7	333.5	104.4	584.3
Wave 2 UD	135.9	655.5	–	–
Reference QI	62.2	686.4	64.2	902.4
Wave 1 QI	33.4	237.9	–	–
Wave 2 QI	66.4	465.7	–	–

account only for 25% of the total laminate. Therefore, the presence of waviness has a reduced influence on QI laminates compared to UD laminate. This results suggest, that the drop in stiffness properties for the more pronounced wave 1 is mainly caused by the geometrical deviation of the wave due to a higher amplitude-to-thickness ratio (A/t). The resulting Young's modulus and strengths for quasi-isotropic laminates are summarized in Table 3.

The applied unidirectional load leads to a complex 2D strain state at the observed cross-section due to the presence of the wave. In Fig. 10 the shear strain ε_{xz} distributions of wavy specimens are shown right before and after final damage within two subsequent frames (10 Hz) for a) wave 1 and b) wave 2 under compression and c) wave 1 under tensile load. Regions of high strain coincide well with the occurrence of macroscopic material failure. This is in accordance with [20], who determined that the associated shear stress τ_{13} is the most significant stress component for damage initiation in wavy composites under axial compression.

While compression loads increase the amplitude-to-wavelength ratio, global applied tensile loads straighten the fiber waviness, leading to an increasing stiffness during

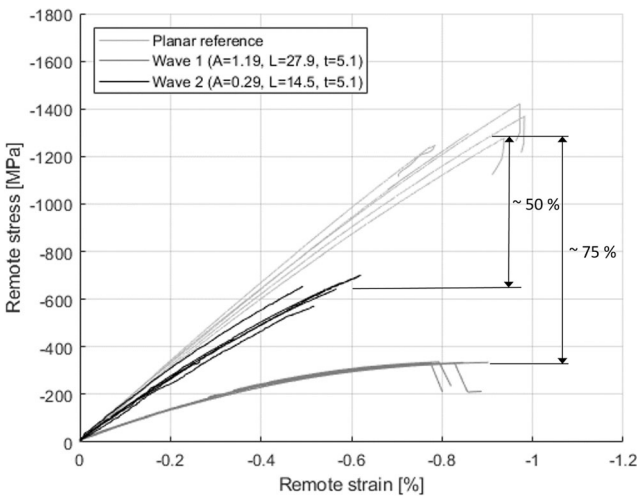

Fig. 7 Compression test of UD-laminate – Comparison planar vs. wavy specimen

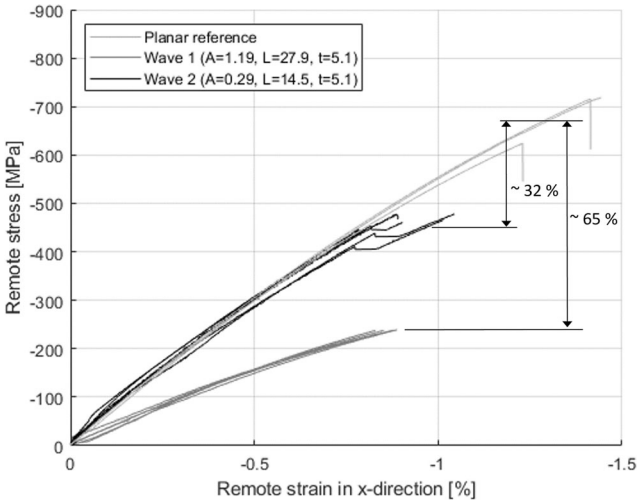

Fig. 8 Compression test of QI-laminate – Comparison planar vs. wavy specimen

loading [57]. Both of which require a geometrically non-linear calculation. The substantial influence of both the amplitude A and thickness t in light of the resulting bending stresses are shown in Eqn. 40. A simplified analytical consideration using the Euler-Bernoulli beam theory (neutral axis coincides with the beam centroid line, bending moment $M_B = FA = \sigma_x\, b\, t\, A$, where A is the amplitude, the moment of inertia for rectangular cross section $J_y = \frac{b\, t^3}{12}$ and $y = \frac{t}{2}$) leads to

$$\sigma_B = \frac{M_B}{J_y} z = \frac{6\, \sigma_x\, A}{t}. \tag{40}$$

Thus, the resulting bending stresses, with a maximum in the longitudinal center of the wave, increases with increasing amplitude and decreases with increasing thickness. To incorporate the geometric non-linearity the curved beam theory can

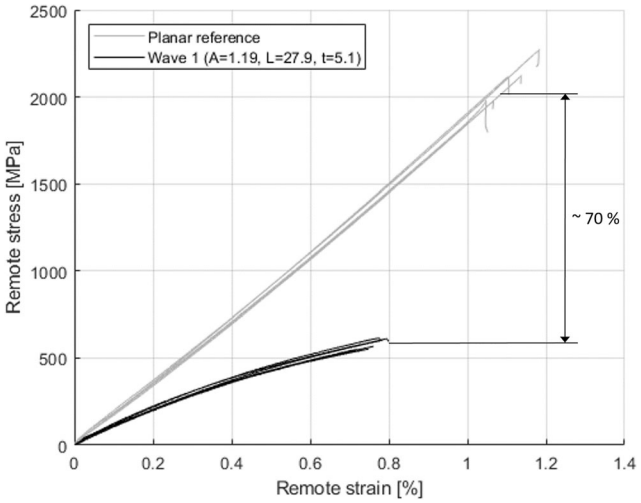

Fig. 9 Tensile test of UD-laminate – Comparison planar vs. wavy specimen

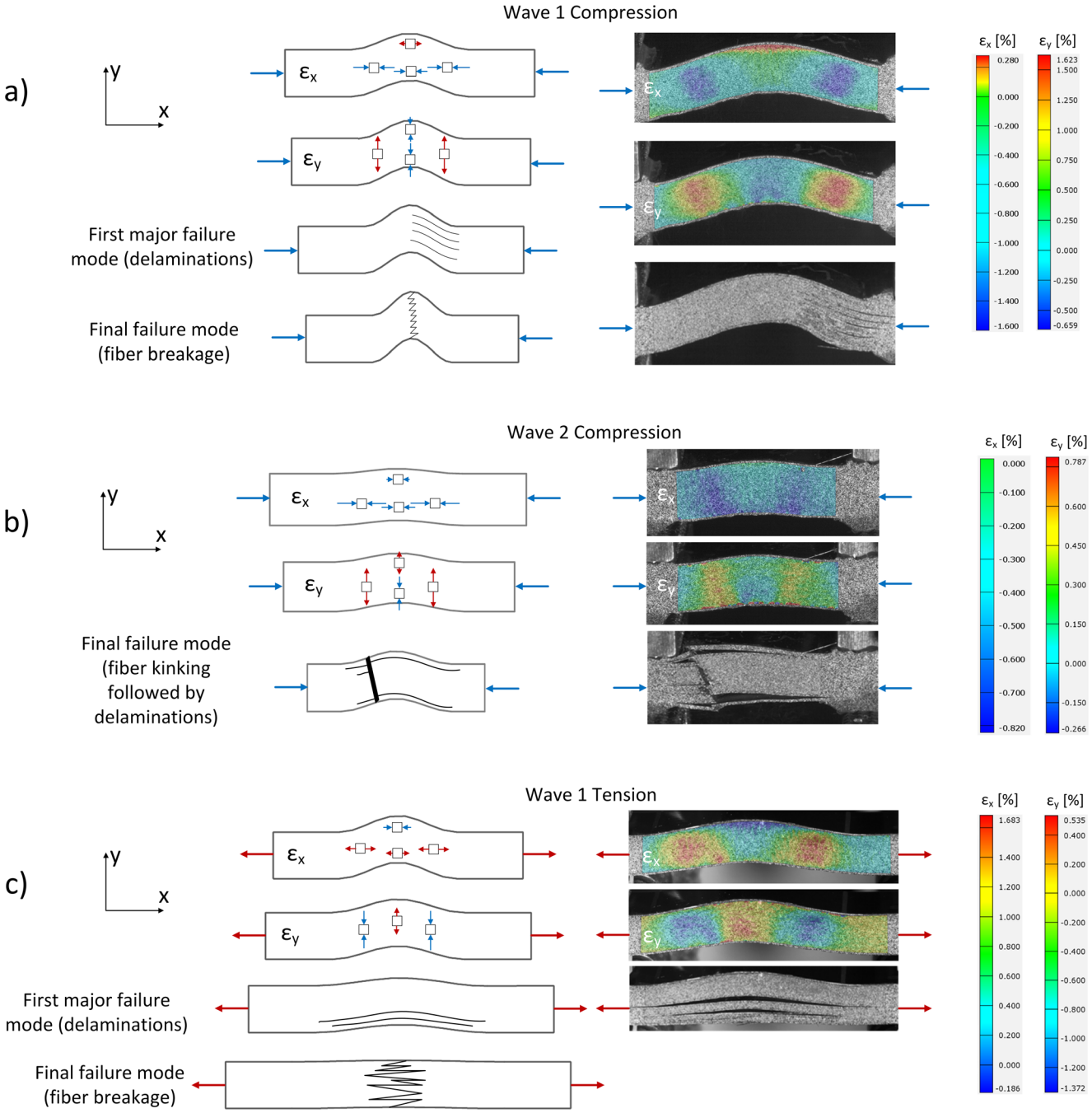

Fig. 13 Schematic illustration and corresponding DIC results of damage behavior including normal strains ε_x and ε_z. **a** wave 1 specimens under compression load; **b**) wave 2 specimens under compression load; **c**) wave 1 specimens under tensile load

be utilized, however a comprehensive analytical study is outside the scope of this contribution.

The resulting shear stress distribution from a linear-elastic but geometrical non-linear FE simulation evaluated along a centroid curve for varying laminate thicknesses, shown in Fig. 11, underlines the thickness-dependent behavior. Shear stresses are highest at the location of the biggest incline/decline and generally increase with thickness. However, when a thickness of *4A* is reached, the further increase of the resulting shear stress is almost zero. An additional linear elastic FE simulation of varying amplitudes and constant wavelength L = 27.9 mm and laminate thickness t = 7.14 mm shows the superposition of bending stresses with the global compressive or tensile load in Fig. 12 by plotting the stresses in x-direction at the peak point of the wavy specimen. This results in different stress states (tension or compression) in the center of the wavy region, depending on the thickness. The compression loaded wave with an amplitude of A = 0.595 mm

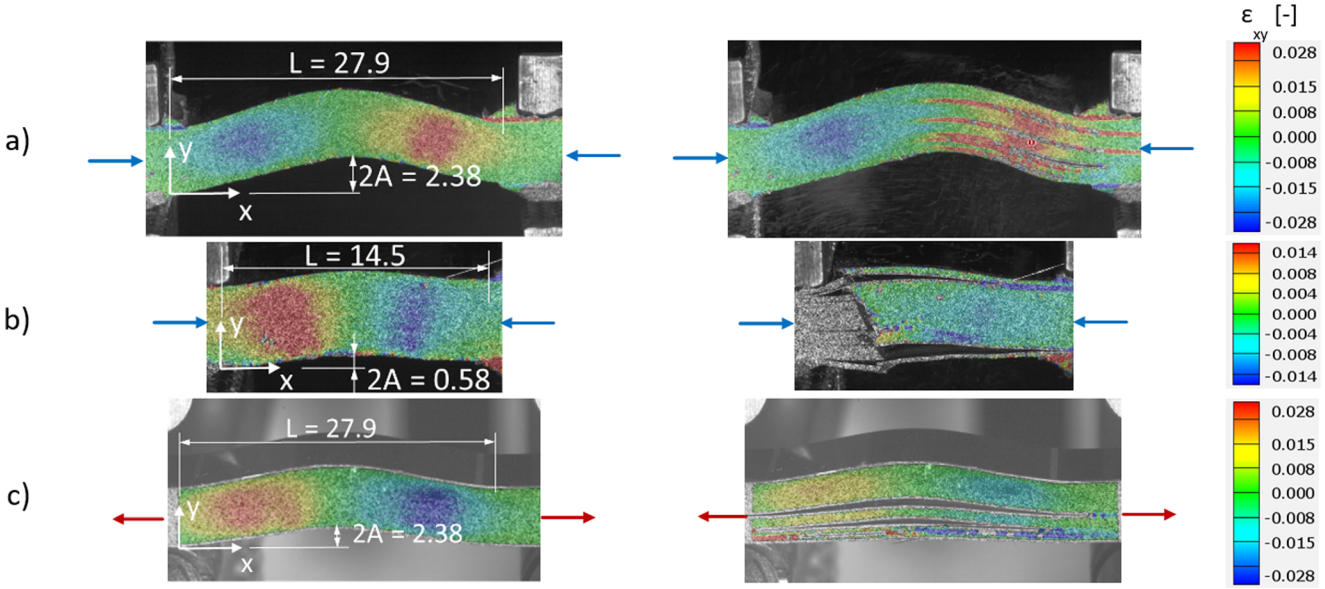

Fig. 10 Shear strain ε_{xz} distribution in the frame captured right before and after macroscopic damage for UD specimen configurations. Blue and red arrows indicate the global loading. **a** wave 1 in compression; **b** wave 2 in compression; **c** wave 1 in tension

shows approximately zero stress σ_x at the peak point due to the superposition of global loading and resulting bending stresses. This mechanism in form of variations of the longitudinal strain component ε_x is also schematically shown in Fig. 13 and can be clearly observed in DIC measurements. There is a transition from tension to compression of ε_x across the thickness when global compression and tension is applied within the tested wave with the higher amplitude (wave 1, c.f. Fig. 13a). Wave 2 (less pronounced waviness) shows a gradient in the strain component but no transition from tensile to compression strains. The effect of superposing bending stresses is amplified during compression testing due to an increasing amplitude-to-wavelength ratio (A/L).

In addition to the above mentioned shear strains that are influencing the failure behavior considerably, resulting tensile strains ε_z, respectively stresses in thickness direction σ_z potentially cause the individual layers to lift off, causing delamination, as shown in Fig. 13a and c). This leads to the conclusion, that the resulting stresses superpose with shear stress components and also considerably influence the failure behavior. In global tensile loading (Fig. 13c), the resulting through thickness strain component ε_z in wave 1 shows a maximum in tension at the center of the wave, leading to delamination along the whole wave length, potentially initiated at the wave center. Wave 2 shows a maximum tensile strain component ε_z at the turning point of the sinusoidal wave under compression loading. This leads to one-sided delamination initiated at the

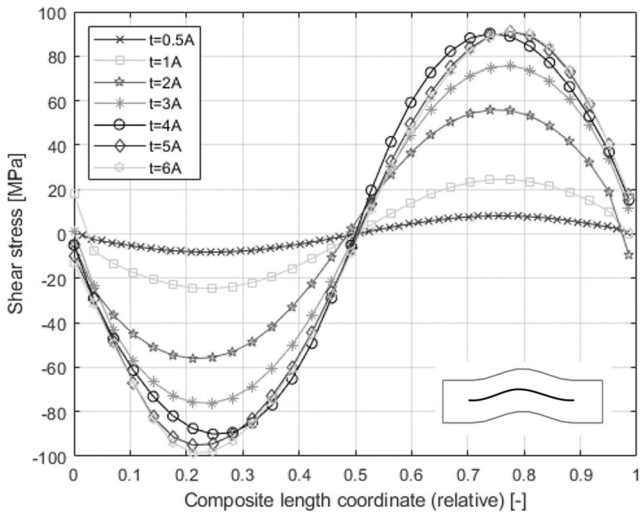

Fig. 11 Shear stress distribution along centroid curve for wave 1 (A = 1.19 mm, L = 27.9 mm) with varying thickness from linear FE-Simulation

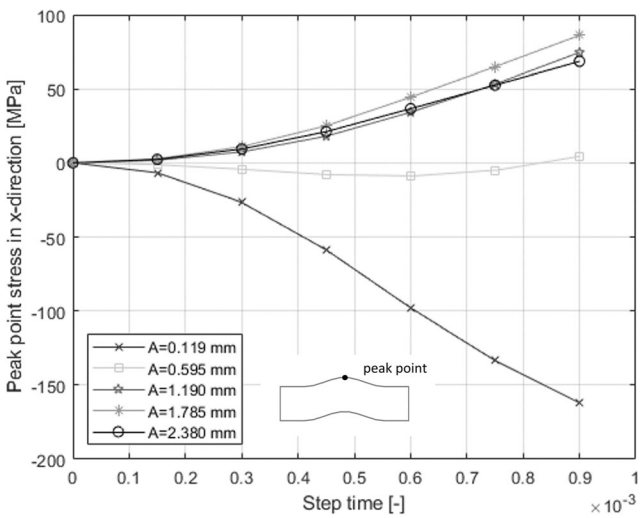

Fig. 12 Peak point stress in x-direction (L = 27.9 mm, t = 7.14 mm) from linear FE-Simulation

area of maximum inclination of the sine wave. Global compression load of wave 2 and the absence of notable bending moments leads to fiber kinking of the specimen schematically depicted in Fig. 13b). The positive strain ε_z in thickness direction leads to less supported fibers and therefore promote the appearance of kink bands. These results suggest that the failure of wave 1 is determined by the bending moments resulting from the geometry (mainly amplitude and thickness). In contrast, for wave 2, the contribution of bending stresses in superposition with the global load is less thus we observe material failure. The failure behavior is more determined by the material properties for lower amplitude-to-thickness ratios.

Model validation

Off-axis tension tests are carried out to determine material parameter needed to describe the nonlinear behavior in combined transverse tension and in-plane shear. According to Körber [58], 15° off-axis specimens are most suitable for the determination of shear properties. In off-axis tests with straight end tabs, it was found that the extension-shear coupling leads to significant stress concentrations near the clamping regions and to a non-uniform strain field. To avoid this, oblique end-tabs were used as proposed by Sun and Chung [59]. The stress-strain response from both simulation and test data for 15° off-axis tensile tests is shown in Fig. 14.

The numerical model is able to match the nonlinear material behavior and the damage initiation properly. However, the resulting failure strain/stress was typically too low, thus our model serves as a conservative estimate. Remote stress-strain curves stemming from simulation and experimental results are shown for wave 1 and wave 2 under compressive loading in Figs. 15 and 16, respectively. The shear strain distribution for wave 1 shows excellent agreement of numerical and experimental results. The global stress-strain relationship for wave 2,

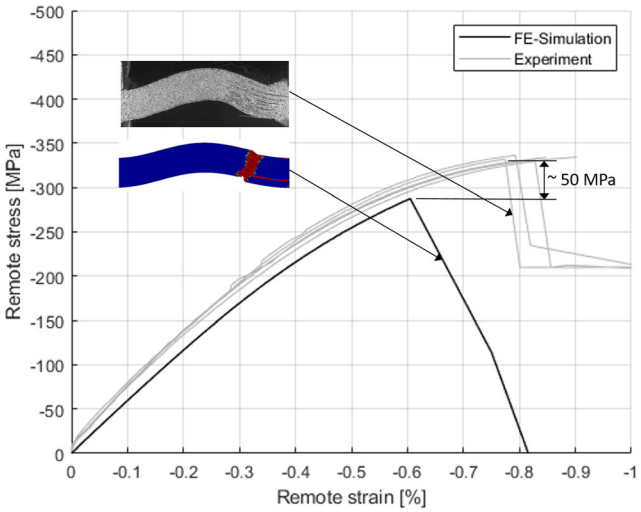

Fig. 15 Experimental and FE analysis results for wave 1 with UD laminate under compression (A = 1.19 mm, L = 27.9 mm, t = 5.1 mm)

including the onset of failure, location and failure pattern shows excellent agreement of simulation and test data.

The typical failure mechanism of a narrow kink-band formation due to matrix yield under compressive loading are indicated at locations of maximum inclinations. The nonlinear stress-strain response is increased at higher remote strains. In Fig. 15 a slightly conservative damage initiation at approximately 50 MPa below test results is probably due to the use of stress-based failure criteria. When the stress-strain curve becomes strongly nonlinear and reaching a plateau, the exact point of damage initiation is more difficult to find. A slight increase in stress leads to a considerable increase in elongation, thus strain-based criteria might be advantageous. The numerical model result is compared with experimental results, determined by digital image correlation (DIC), by comparing the shear strain distribution along the center line of the wave in Fig. 17.

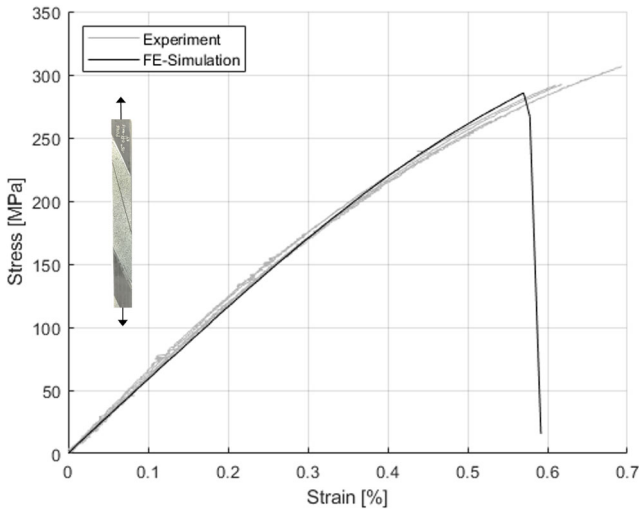

Fig. 14 Experimental and FE analysis results for 15° off-axis tensile test (OAT)

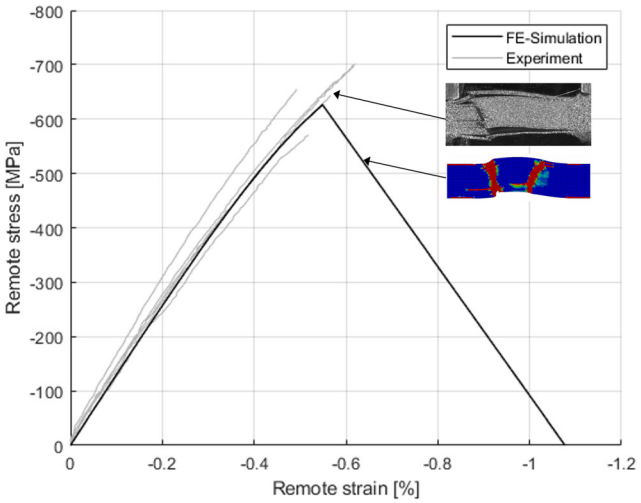

Fig. 16 Experimental and FE analysis results for wave 2 with UD laminate under compression (A = 0.29 mm, L = 14.5 mm, t = 5.1 mm)

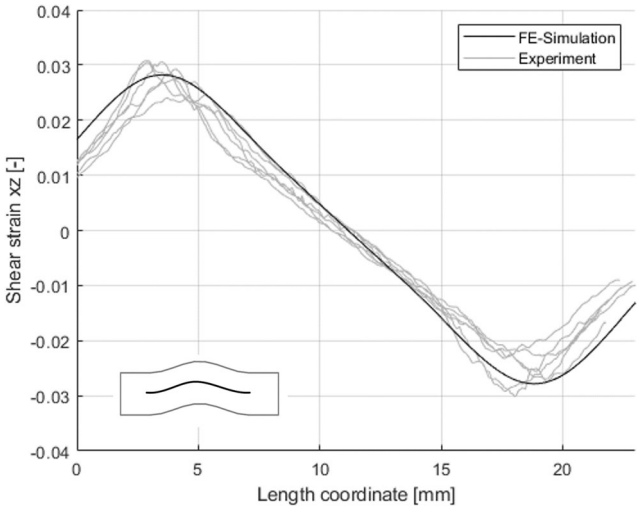

Fig. 17 Shear strain ε_{xz} of wave 1 with UD laminate under compression along curve

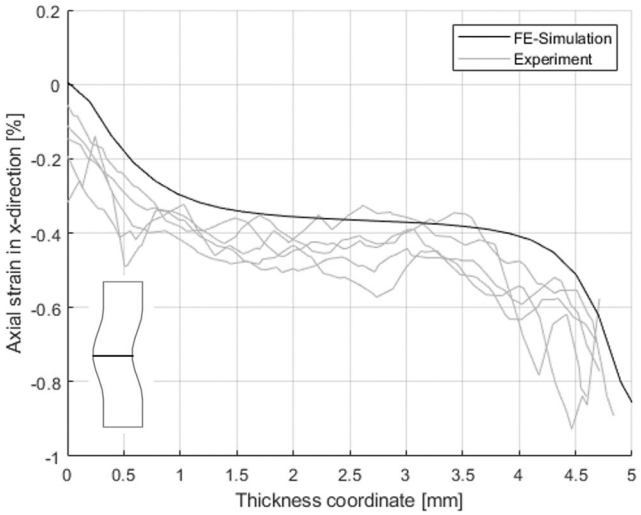

Fig. 19 Axial strain in x-direction ε_x of wave 2 with UD laminate under compression center line

The axial strain ε_x from our simulations and the DIC measurements evaluated along a centered path vertical to the loading direction shows good agreement of numerical and experimental data for both wave configurations with UD laminate in Figs. 18 and 19.

To evaluate the applicability and limitations of the implemented 2D continuum damage model for more complex materials, it is applied for wave 2 under compressive loading for a quasi-isotropic laminate $(0/45/-45/90)_{5s}$. The global stress-strain response, shown in Fig. 20, can only be reproduced insufficiently. The resulting complex 3D stress state leads to a complex failure behavior of QI laminates that cannot be represented by the 2D model, due to neglecting the stress components in y-direction. However, the resulting failure mode as well as the correct location for damage onset were detected correctly at the center of the wave. For the simulation of QI laminates, the model can merely be used as an engineering estimation of the material properties and a qualitative assessment of failure. Therefore, for analyzing QI laminates containing fiber waviness an extension to a three-dimensional model which incorporates nonlinearity parameter for various ply orientations, fiber rotation and cohesive layers for modeling delamination is suggested.

Virtual testing

The model has been successfully validated for UD materials. To reduce the effort of physical testing the model is applied for studying the influence of varying parameters, e.g. amplitudes A, thicknesses t and wavelengths L, in the sense of a virtual test approach. The considerable influence of laminate thickness on the failure behavior has already been described in Section 4.1. The virtual testing

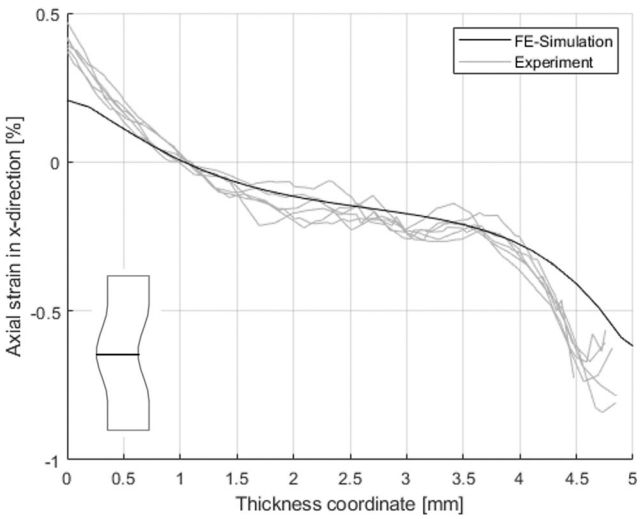

Fig. 18 Axial strain in x-direction ε_x of wave 1 with UD laminate under compression center line

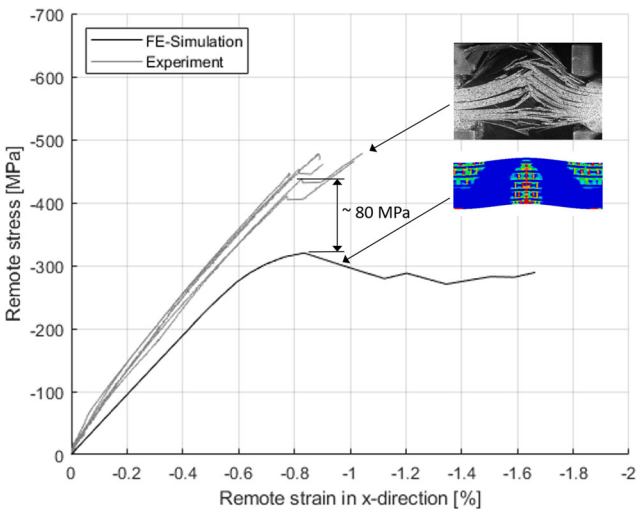

Fig. 20 Experimental and FE analysis results for wave 2 with QI laminate under compression (A = 0.29 mm, L = 14.5 mm, t = 5.1 mm)

results, shown in Fig. 21, illustrate the shift from failure dominated by bending stresses to the formation of kink bands with increasing laminate thickness. This confirms our statement, that for lower A/t ratios the testing regime represents a test at material level, whereas the failure behavior above a certain threshold for A/t ratios is strongly influenced by introduced bending moments, thus representing a test on structural level. This results in a pronounced non-linearity in the stress-strain curve of thin laminates (e.g. t = 0.5A and t = 1A) due to the influence of the geometry (geometrical non-linearity).

Figure 22 shows the global stress-strain response of compression loaded waviness with varying amplitudes and constant thickness (t = 7.14 mm) and wavelength (L = 27.9 mm). Even minor fiber deviations associated with the amplitude lead to a drastic reduction of the mechanical properties, which is known from transformation relations for engineering constants as a function of different fiber orientations [60]. According to that, simulation results show the relative reduction of the stiffness to be smaller at higher amplitudes.

The results from FE simulations of waves with varying wavelength and constant amplitude (A = 1.19 mm) and thickness (t = 7.14 mm), shown in Fig. 23. The relative drop in compressive strength from L = 41.35 mm to L = 13.45 mm is ~46%. However, compared to a planar reference specimen those specimens show a reduction of 76% (L = 41.35 mm) and 87% (L = 13.45 mm, thus only a 11% absolute difference. This confirms to Lemanski and Sutcliffe [27], who stated that the effect of defect length is relatively small in this configuration.

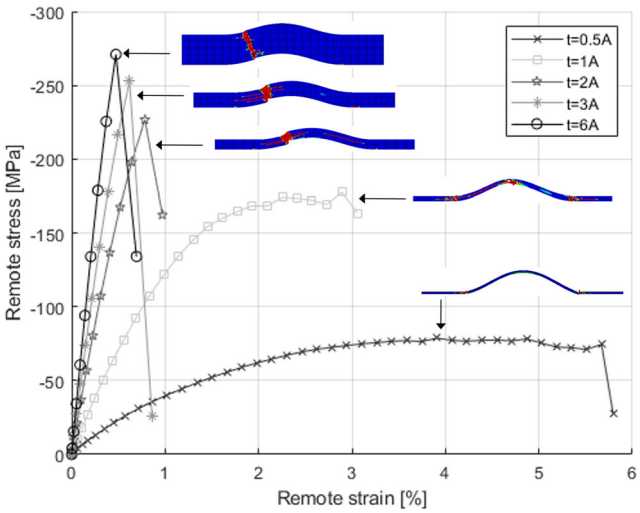

Fig. 21 Stress-strain relationship for wavy specimen (A = 1.19 mm, L = 27.9 mm) with UD laminate and varying thickness using implemented non-linear VUMAT (Puck)

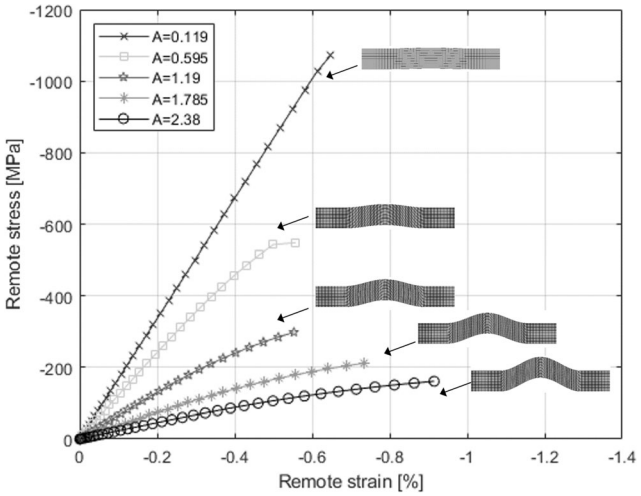

Fig. 22 Stress-strain relationship for wavy specimen (t = 7.14 mm, L = 27.9 mm) with UD laminate and varying amplitude using implemented non-linear VUMAT (Puck)

Conclusions and outlook

We successfully tested and simulated the mechanical behavior and damage initiation for two wave configurations with UD and QI laminates under compressive and tensile loading. The understanding of intrinsic material behavior of fiber reinforced composite materials on microscopic level up to macroscopic or structural level is of crucial importance for the development of suitable material laws for numerical modeling and for a deeper understanding of deformation and damage mechanisms. On top of that, understanding the material behavior of wavy composites is of vital importance for further cost and weight savings. The implemented nonlinear material model was able to capture the material behavior including shear nonlinearities, failure initiation and propagation in unidirectional

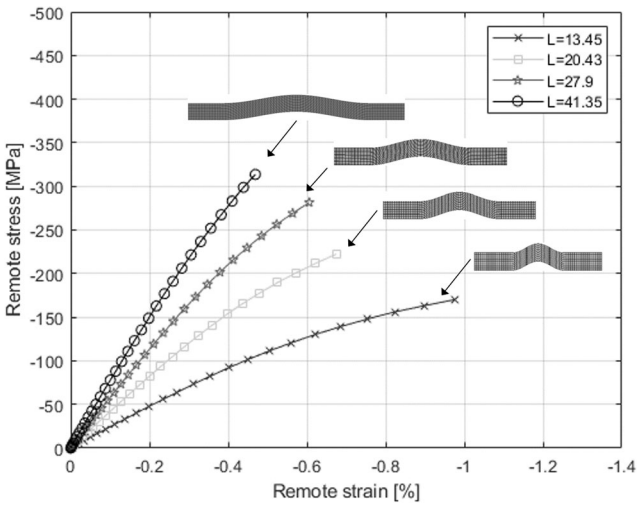

Fig. 23 Stress-strain relationship for wavy specimen (A = 1.19 mm, t = 7.14 mm) with UD laminate and varying wavelength using implemented non-linear VUMAT (Puck)

laminates reasonably accurate. Overall, our results suggest that, depending on the laminate configuration (amplitude, wavelength, thickness) inter-laminar shear failure is the dominant failure mechanism followed by mode I delamination and layer-wise buckling. The nonlinear shear behavior under compressive loading increases with the severity of present fiber waviness and, therefore, plays a dominant role for the initiation and propagation of the failure mechanisms. For wave configurations with a lower amplitude-to-thickness ratio fiber kinking is the dominant failure mechanism under compression loading. The observed formation of a shear kink-band under compression and shear stress (Fig. 10b) is caused by local fiber buckling, induced by misaligned fibers in the UD materials that continue to rotate under load. In this work, the significant influence of laminate thickness was shown, which has been rarely considered in both industrial practice and academic research so far. The failure behavior for lower amplitude-to-thickness ratios is more determined by the material properties, whereas higher amplitude-to-thickness ratios lead to a higher influence of the geometry due to bending. For this reason, we suggest to consider the amplitude-to-thickness ratio (A/t) in addition to the commonly used ratio of amplitude-to-wavelength (A/L) for further assessment strategies of fiber waviness. The validity of the model applies for quasi-static loaded unidirectional laminates only. For multidirectional laminates an extension from 2D to 3D is necessary to incorporate the complex 3D stress state.

Acknowledgements The Austrian Research Promotion Agency (FFG) is gratefully acknowledged for funding this research in the BRIDGE 1 program (Project FiberWave; Grant No. 855711). The authors are also pleased to express their grateful acknowledgements to the cooperation partner FACC Operations GmbH.

Funding Information Open access funding provided by University of Applied Sciences Upper Austria.

Compliance with ethical standards

Conflict of interest The authors declare that they have no conflict of interest.

References

1. Potter K, Khan B, Wisnom M, Bell T, Stevens J (2008) Variability, fibre waviness and misalignment in the determination of the properties of composite materials and structures. Compos Part A Appl Sci Manuf 39:1343–1354. https://doi.org/10.1016/j.compositesa.2008.04.016
2. Potter KD (2009) Understanding the origins of defects and variability in composites manufacture. 17 Th Int Conf Compos Mater:27–31
3. Nelson JW, Riddle TW, Cairns DS, Investigator P. Effects of defects in composite wind turbine blades : round 1 2012
4. Davidson P, Waas AM (2012) Effect of Fiber Waviness on the Compressive Strength of Unidirectional Carbon Fiber Composites. 53rd AIAA/ASME/ASCE/AHS/ASC. Struct Struct Dyn Mater Conf:1–16
5. Hsiao HM, Daniel IM (1996) Effect of fiber waviness on stiffness and strength reduction of unidirectional composites under compressive loading. Compos Sci Technol 56:581–593. https://doi.org/10.1016/0266-3538(96)00045-0
6. Cimini Jr. CA, Tsai SW. Ply Waviness on in-Plane Stiffness of Composite Laminates. 12th Int Conf Compos Mater n.d.
7. El-Hajjar RF, Petersen DR (2011) Gaussian function characterization of unnotched tension behavior in a carbon/epoxy composite containing localized fiber waviness. Compos Struct 93:2400–2408. https://doi.org/10.1016/j.compstruct.2011.03.029
8. Caiazzo A, Orlet M, McShane H, Strait L, Rachau C (2000) The effects of marcel defects on composite structural properties. Compos Struct Theory Pract 1383:158–187. https://doi.org/10.1520/Stp14509s
9. Creighton CJ, Sutcliffe MPF, Clyne TW (2001) Multiple field image analysis procedure for characterization of fibre alignment in composites. Compos Part A Appl Sci Manuf 32:221–229. https://doi.org/10.1016/S1359-835X(00)00115-9
10. Sutcliffe MPF, Lemanski SL, Scott AE (2012) Measurement of fibre waviness in industrial composite components. Compos Sci Technol 72:2016–2023. https://doi.org/10.1016/j.compscitech.2012.09.001
11. Nikishkov G, Nikishkov Y, Makeev A (2013) Finite element mesh generation for composites with ply waviness based on X-ray computed tomography. Adv Eng Softw 58:35–44. https://doi.org/10.1016/j.advengsoft.2013.01.002
12. Lightfoot JS, Wisnom MR, Potter K (2013) A new mechanism for the formation of ply wrinkles due to shear between plies. Compos Part A Appl Sci Manuf 49:139–147. https://doi.org/10.1016/j.compositesa.2013.03.002
13. Lightfoot JS, Wisnom MR, Potter K (2013) Defects in woven preforms: formation mechanisms and the effects of laminate design and layup protocol. Compos Part A Appl Sci Manuf 51:99–107. https://doi.org/10.1016/j.compositesa.2013.04.004
14. Lukaszewicz DHJA, Ward C, Potter KD (2012) The engineering aspects of automated prepreg layup: history, present and future. Compos Part B Eng 43:997–1009. https://doi.org/10.1016/j.compositesb.2011.12.003
15. Croft K, Lessard L, Pasini D, Hojjati M, Chen J, Yousefpour A (2011) Experimental study of the effect of automated fiber placement induced defects on performance of composite laminates. Compos Part A Appl Sci Manuf 42:484–491. https://doi.org/10.1016/j.compositesa.2011.01.007
16. Belnoue JPH, Mesogitis T, Nixon-Pearson OJ, Kratz J, Ivanov DS, Partridge IK et al (2017) Understanding and predicting defect formation in automated fibre placement pre-preg laminates. Compos Part A Appl Sci Manuf 102:196–206. https://doi.org/10.1016/j.compositesa.2017.08.008

17. Boisse P, Colmars J, Hamila N, Naouar N, Steer Q (2018) Bending and wrinkling of composite fiber preforms and prepregs. A review and new developments in the draping simulations. Compos Part B Eng 141:234–249. https://doi.org/10.1016/j.compositesb.2017.12.061
18. Sjölander J, Hallander P, Åkermo M (2016) Forming induced wrinkling of composite laminates: a numerical study on wrinkling mechanisms. Compos Part A Appl Sci Manuf 81:41–51. https://doi.org/10.1016/j.compositesa.2015.10.012
19. Budiansky B (1994) Fleck N a. Compressive Kinking of Fiber Composites: A Topical Review Appl Mech Rev 47:S246. https://doi.org/10.1115/1.3124417
20. Hsiao HM, Daniel IM (1996) Elastic properties of composites with fiber waviness. Compos Part A Appl Sci Manuf 27:931–940. https://doi.org/10.1016/1359-835X(96)00034-6
21. Piggott MR (1995) The effect of fibre waviness on the mechanical properties of unidirectional fibre composites: a review. Compos Sci Technol 53:201–205. https://doi.org/10.1016/0266-3538(95)00019-4
22. Altmann A, Taubert R, Mandel U, Hinterhoelzl R, Drechsler K (2015) A continuum damage model to predict the influence of ply waviness on stiffness and strength in ultra-thick unidirectional Fiber-reinforced Plastics. J Compos Mater:0021998315612536. https://doi.org/10.1177/0021998315612536
23. Adams DOH, Bell SJ (1995) Compression strength reductions in composite laminates due to multiple-layer waviness. Compos Sci Technol 53:207–212. https://doi.org/10.1016/0266-3538(95)00020-8
24. Steeves CA, Fleck NA (2005) Compressive strength of composite laminates with terminated internal plies. Compos Part A Appl Sci Manuf 36:798–805. https://doi.org/10.1016/j.compositesa.2004.10.024
25. Wang J, Potter KD, Etches J (2013) Experimental investigation and characterisation techniques of compressive fatigue failure of composites with fibre waviness at ply drops. Compos Struct 100:398–403. https://doi.org/10.1016/j.compstruct.2013.01.010
26. Elhajjar RF (2014) Shams SS. Compression testing of continuous fiber reinforced polymer composites with out-of-plane fi ber waviness and circular notches 35:45–55
27. Lemanski SL, Sutcliffe MPF (2012) Compressive failure of finite size unidirectional composite laminates with a region of fibre waviness. Compos Part A Appl Sci Manuf 43:435–444. https://doi.org/10.1016/j.compositesa.2011.11.007
28. Zhu J, Wang J, Zu L (2015) Influence of out-of-plane ply waviness on elastic properties of composite laminates under uniaxial loading. Compos Struct 132:440–450. https://doi.org/10.1016/j.compstruct.2015.05.062
29. Li Y, Stier B, Bednarcyk B, Simon JW, Reese S (2016) The effect of fiber misalignment on the homogenized properties of unidirectional fiber reinforced composites. Mech Mater 92:261–274. https://doi.org/10.1016/j.mechmat.2015.10.002
30. Vogler TJ, Hsu S-Y, Kyriakides S (2000) Composite failure under combined compression and shear. Int J Solids Struct 37:1765–1791. https://doi.org/10.1016/S0020-7683(98)00323-0
31. Pinho ST, Iannucci L, Robinson P. Physically based failure models and criteria for laminated fibre-reinforced composites with emphasis on fibre kinking. Part II: FE implementation. Compos Part A Appl Sci Manuf 2006. https://doi.org/10.1016/j.compositesa.2005.06.008
32. Pinho ST, Iannucci L, Robinson P (2006) Physically-based failure models and criteria for laminated fibre-reinforced composites with emphasis on fibre kinking: part I: development. Compos Part A Appl Sci Manuf 37:63–73. https://doi.org/10.1016/j.compositesa.2005.04.016
33. Budiansky B, Fleck NA (1993) Compressive failure of fibre composites. J Mech Phys Solids 41:183–211. https://doi.org/10.1016/0022-5096(93)90068-Q
34. Jelf PM, Fleck NA (1992) Compression failure mechanisms in unidirectional composites. J Compos Mater 26:2706–2726. https://doi.org/10.1177/002199839202601804
35. Niu K, Talreja R (2000) Modeling of compressive failure in fiber reinforced composites. Int J Solids Struct 37:2405–2428. https://doi.org/10.1016/S0020-7683(99)00010-4
36. Slaughter WS, Fleck NA (1994) Microbuckling of fiber composites with random initial fiber waviness. J Mech Phys Solids 42:1743–1766. https://doi.org/10.1016/0022-5096(94)90070-1
37. Lemanski SL, Wang J, Sutcliffe MPF, Potter KD, Wisnom MR (2013) Modelling failure of composite specimens with defects under compression loading. Compos Part A Appl Sci Manuf 48:26–36. https://doi.org/10.1016/j.compositesa.2012.12.007
38. Daniel IM, Luo JJ, Schubel PM, Werner BT (2009) Interfiber/interlaminar failure of composites under multi-axial states of stress. Compos Sci Technol 69:764–771. https://doi.org/10.1016/j.compscitech.2008.04.016
39. Bogetti TA, Gillespie JW, Lamontia MA (1994) The influence of ply waviness with nonlinear shear on the stiffness and strength reduction of composite laminates. J Thermoplast Compos Mater 7:76–90. https://doi.org/10.1177/089270579400700201
40. Pimenta S, Gutkin R, Pinho ST, Robinson P (2009) A micromechanical model for kink-band formation: part I — experimental study and numerical modelling. Compos Sci Technol 69:948–955. https://doi.org/10.1016/j.compscitech.2009.02.010
41. Pimenta S, Gutkin R, Pinho ST, Robinson P (2009) A micromechanical model for kink-band formation: part II—analytical modelling. Compos Sci Technol 69:956–964. https://doi.org/10.1016/j.compscitech.2009.02.003
42. Hinton MJ, Kaddour AS, Soden PD. The world-wide failure exercise. Elsevier Science Ltd.; 2004
43. Chun H, Shin J, Daniel IM. Effects of material and geometric nonlinearities on the tensile and compressive behavior of composite materials with fiber waviness 2001;61:125–134
44. Altmann A, Gesell P, Drechsler K (2015) Strength prediction of ply waviness in composite materials considering matrix dominated effects. Compos Struct 127:51–59. https://doi.org/10.1016/j.compstruct.2015.02.024
45. Lan M, Cartié D, Davies P, Baley C (2016) Influence of embedded gap and overlap fiber placement defects on the microstructure and shear and compression properties of carbon-epoxy laminates. Compos Part A Appl Sci Manuf 82:198–207. https://doi.org/10.1016/j.compositesa.2015.12.007
46. Wisnom MR (1994) Shear fracture of unidirectional composites without initial cracks 52:9–17
47. Bloom LD, Wang J, Potter KD (2013) Damage progression and defect sensitivity: an experimental study of representative wrinkles in tension. Compos Part B Eng 45:449–458. https://doi.org/10.1016/j.compositesb.2012.05.021
48. Mukhopadhyay S, Jones MI, Hallett SR (2015) Compressive failure of laminates containing an embedded wrinkle; experimental and numerical study. Compos Part A Appl Sci Manuf 73:132–142. https://doi.org/10.1016/j.compositesa.2015.03.012
49. Mukhopadhyay S, Jones MI, Hallett SR (2015) Tensile failure of laminates containing an embedded wrinkle; numerical and experimental study. Compos Part A Appl Sci Manuf 77:219–228. https://doi.org/10.1016/j.compositesa.2015.07.007
50. Mukhopadhyay S, Nixon-Pearson OJ, Hallett SR (2018) An experimental and numerical study on fatigue damage development in laminates containing embedded wrinkle defects. Int J Fatigue 107:1–12. https://doi.org/10.1016/j.ijfatigue.2017.10.008

51. Wilhelmsson D, Asp LE, Gutkin R, Edgren F (2017) Fibre waviness induced bending in compression tests of uniderectional NCF composites. ICCM Int Conf Compos Mater 2017:20–25
52. Corp DSS (2017) Abaqus analysis User's guide, version 2017. USA, Providence
53. Puck A, Schürmann H (2004) Failure analysis of FRP laminates by means of physically based phenomenological models. Fail Criteria Fibre-Reinforced-Polymer Compos. https://doi.org/10.1016/B978-008044475-8/50028-7
54. Sun CT, Chen JL (1989) A simple flow rule for characterizing nonlinear behavior of Fiber composites. J Compos Mater. https://doi.org/10.1177/002199838902301004
55. Coleman BD, Gurtin ME (1967) Thermodynamics with internal state variables. J Chem Phys. https://doi.org/10.1063/1.1711937
56. Maimí P, Camanho PP, Mayugo JA, Dávila CG (2007) A continuum damage model for composite laminates: part II – computational implementation and validation. Mech Mater 39:909–919. https://doi.org/10.1016/j.mechmat.2007.03.006
57. Garnich MR, Karami G (2004) Finite element micromechanies for stiffness and strength of wavy fiber composites. J Compos Mater 38:273–292. https://doi.org/10.1177/0021998304039270
58. Körber H (2010) Mechanical response of advanced composites under high strain rates. University of Porto
59. Sun CT, Chung I (1993) An oblique end-tab design for testing off-axis composite specimens. Composites 24:614–623. https://doi.org/10.1016/0010-4361(93)90124-Q
60. Daniel IM, Ishai O (1994) Engineering mechanics of composite materials. Mech Compos Mater:881–886. https://doi.org/10.1016/B978-0-08-006421-5.50049-6
61. Camanho PP, Maimí P, Dávila CG (2007) Prediction of size effects in notched laminates using continuum damage mechanics. Compos Sci Technol. https://doi.org/10.1016/j.compscitech.2007.02.005
62. Mandel U, Taubert R, Hinterhölzl R (2015) Mechanism based nonlinear constitutive model for composite laminates subjected to large deformations. Compos Struct 132:98–108. https://doi.org/10.1016/j.compstruct.2015.04.029
63. Puck A, Kopp J, Knops M (2002) Guidelines for the determination of the parameters in Puck's action plane strength criterion. Compos Sci Technol. https://doi.org/10.1016/S0266-3538(01)00202-0
64. Mandel U, Taubert R, Hinterhölzl R (2016) Laminate damage model for composite structures. Compos Struct 136:441–449. https://doi.org/10.1016/j.compstruct.2015.10.032
65. Mandel U. (2016) Mechanism based constitutive model for composite laminates. Technical University of Munich